

Electrically Reconfigurable Mode Chirality in Integrated Microring Resonators

Yihao Chen, Jin Li, Ke Xu,* Stefano Biasi, Riccardo Franchi, Chaoran Huang, Juntao Duan, Xi Wang, Lorenzo Pavesi, Xiaochuan Xu,* and Jiawei Wang*

Chirality, one of the universal phenomena in physics, forms the playground for fascinating phenomena in modern electromagnetism and industrial applications. Within the rapidly advancing technologies of integrated optoelectronic and all-optical devices, controlling the light flow on a chip using optical chiral modes emerges as a crucial topic, which implies numerous counterintuitive chiroptical effects such as unidirectional emission, magnetic-free non-reciprocity, chiral switching, and enhanced sensitivity. Here strong yet reconfigurable mode chirality is demonstrated in integrated silicon-based spiral microring resonators. Leveraging the adjustable azimuthal positions of two spiral edges as asymmetric local scatterers, the inter-modal coupling can be manipulated, which bypasses the requirement of external off-chip components in conventional schemes. Besides, an integrated phase shifter enables electrical reconfiguration of the non-Hermiticity toward or away from exceptional points. Experimental results reveal post-fabrication reconfiguration with a sign-reversible chirality and chirality-induced suppression of backscattering down to -24 dB. By virtue of demonstrations using standard silicon photonics foundry services, the findings provide a new design framework of microresonators as a building block for integrated chiral photonics in both classical and quantum regimes.

1. Introduction

Chirality naturally exists in the molecular or material structures that possess handedness or asymmetry. In addition, its importance has been long intriguing in modern physics, especially topological states,^[1] spintronics,^[2] and emerging chiral quantum photonics.^[3] Akin to chiral edge states in topological insulators, in optics, secured optical chirality suggests a forbidden propagation of photons in the opposite direction, which leads to fascinating phenomena such as photonic Aharonov–Bohm effect,^[4] magnetic-free nonreciprocity,^[5] unidirectional emission,^[6] chiral light-matter interaction,^[6,7] asymmetric mode switching,^[8] and so on. In recent years, whispering gallery mode (WGM) microresonators have been widely investigated as an open physical system for studying chiral photonics and non-Hermitian photonics.^[9–12] In the sense of transverse spin angular momentum carried by lightwaves circulating in a WGM cavity, propagations in the clockwise (CW) and the counter-clockwise (CCW) directions carry distinct chirality.^[13] Harnessing the broken chiral symmetry, exotic properties of optical resonant fields open up new possibilities with even counterintuitive features, such as unidirectional emission,^[9,14,15] reconfigurable symmetry-broken lasers,^[16,17] generation of tunable orbital angular momentum,^[18,19] enhanced sensing,^[5,20,21] and chiral perfect absorption.^[7,22]

The chirality of optical WGMs can be mediated simply via inter-modal coupling between two naturally existing near-degenerate resonant modes, in which adjusting the optical gain/loss condition is no longer a prerequisite. The mode chirality reaches its maximum at an exceptional point (EP), where two (or multiple) eigenvalues and the associated eigenstates coalesce.^[23–25] Apart from the reported reconfigurable chirality in lasing,^[16,17] steering of non-Hermitian spectral degeneracies, and effective mode chirality, has been pioneered using the “two-scatterers” strategy,^[24,26–29] in which the relative positions of two external nano scatterers are judiciously controlled around the cavity for perturbing the evanescent field and maneuvering the induced inter-modal coupling. Despite the high accuracy of this well-established scheme, precision off-chip equipment

Y. Chen, J. Li, K. Xu, J. Duan, X. Wang, X. Xu, J. Wang
School of Electronic and Information Engineering
Harbin Institute of Technology (Shenzhen)
Shenzhen 518055, China
E-mail: kxu@hit.edu.cn; xuxiaochuan@hit.edu.cn; wangjw7@hit.edu.cn

K. Xu, X. Xu, J. Wang
State Key Laboratory on Tunable Laser Technology
Harbin Institute of Technology (Shenzhen)
Shenzhen 518055, China

S. Biasi, R. Franchi, L. Pavesi
Nanoscience Laboratory
Dipartimento di Fisica
Università di Trento
Trento 38123, Italy

C. Huang
Department of Electronic Engineering
The Chinese University of Hong Kong
Hong Kong 999077, China

 The ORCID identification number(s) for the author(s) of this article can be found under <https://doi.org/10.1002/lpor.202301289>

DOI: [10.1002/lpor.202301289](https://doi.org/10.1002/lpor.202301289)

(mainly nanotips and nanopositioners) cannot be avoided,^[28,30,31] which significantly plagued the technology transfer into prospective applications especially in the burgeoning industry of integrated photonics. For on-chip densely integrated planar microresonators, mode chirality can be controlled by generating highly unbalanced backscattering strength between CW and CCW lightwaves using two approaches. The first one is to introduce lithographically patterned scatterers (e.g., nanonotches^[32] and nanoparticles^[33]) with deliberately controlled shapes, sizes, and locations. The second one is to employ extra on-chip (e.g., Taiji resonators,^[34,35] infinite-loop resonators,^[36] and resonators with integrated reflectors^[37–39]) or off-chip (e.g., optical isolators^[21] and fiber loop mirror^[7]) components facilitating mode conversion. However, in both approaches, the resulted chirality is fixed to a deterministic value, and the post-fabrication reconfigurability remains elusive. For on-chip waveguide-coupled microring resonators as an extensively exploited building block on various fronts, realizing reconfigurable mode chirality will unleash the potential of chiral devices in both classical and quantum regimes.

In this article, we experimentally demonstrated a, hitherto lacking, framework of integrated optical microresonators with electrically reconfigurable mode chirality. In particular, the scheme has been successfully realized solely by on-chip integrated elements based on silicon photonics foundry processes, which is in contrast with previously demonstrated chirality tuning schemes leveraging off-chip components.^[26,30] In the proposed spiral ring system, the azimuthal spacing between two spiral edges serves as a generic knob to manipulate the mode chirality between the CCW/CW-dominated regimes. Strong mode chirality up to ≈ 0.86 was experimentally demonstrated, which counterbalances the intrinsic Rayleigh scattering in regular microrings with weak chirality, and results in coherent suppression of backscattering down to ≈ -24 dB. Besides, localized thermo-optic tuning enables a post-fabrication approach to steer around a chiral state toward or away from EPs. The observed sign-reversible chirality verifies the reconfigurability. The proof-of-concept demonstration using silicon nitride microring resonators in the submicrometer wavelengths is of great significance to their emerging applications,^[40,41] from sensing,^[42] to data centers, to neural networks, to Lidar,^[40] and to quantum photonics.

2. Results

2.1. Working Principles

For analyses of perturbed modes in microrings, usually, an effective Hamiltonian as a 2×2 matrix is introduced,^[43,44]

$$H = \begin{pmatrix} \Omega & A \\ B & \Omega \end{pmatrix} \quad (1)$$

The diagonal elements describe original modes in the traveling-wave basis, including the energy (real part) and the decay rate (imaginary part), while the off-diagonal elements describe the coherent backscattering of light from CW to CCW (**A**) and from CCW to CW (**B**) direction. To generate backscattering inside a microring, a simple and intuitive way is to introduce a

“protruded” segment along the radial direction (spanning an azimuthal angle θ , see the left panel of Figure 1a). A mismatch in the lateral dimension in a waveguiding system leads to nonconservative coupling of counter-propagating waves, impacting both **A** and **B**. Due to the preserved structural symmetry, the contributions of **A** and **B** are balanced. Tuning θ may effectively steer the system to break the mode degeneracy (see the left panel of Figure 1b). However, the mode chirality remains to be weak.

A simple yet efficient way to break the mirror symmetry in a ring is to utilize the spiral shape, which can be viewed as curving one waveguide into a loop. Two spiral edges feature a radial offset T and an adjustable relative azimuthal position (i.e., angle θ) describing the overlapping segment of this chopped spiral waveguide with a width of $W + T$ (See the right panel of Figure 1a). Considering the mode delocalization due to bending curvature, the perturbation effects introduced by inner and outer edges might be highly unbalanced. This effect can be quantified using a complex “asymmetric factor” $\chi = (V_{\text{outer}} - U_{\text{outer}})/(V_{\text{inner}} - U_{\text{inner}})$, in which **V** and **U** are the complex mode shifts for positive- and negative-parity modes, respectively, and the subscript labels the corresponding spiral edges (for details, see Section S1, Supporting Information). Under this circumstance, the Hamiltonian matrix becomes non-Hermitian. Hence, the eigenvectors become in general not orthogonal. By adjusting the non-Hermicity using θ and χ , two EPs, namely EP+ (**B** = 0) and EP- (**A** = 0), can be approached (see the right panel of Figure 1b).

In the following studies, the peculiar optical response using an integrated and waveguide-coupled spiral ring was investigated, in which the non-Hermicity and associated mode chirality can be controlled by either adjusting θ at the pre-fabrication stage or local phase tuning at the post-fabrication stage. Leveraging the maturing silicon photonics technology, optically passive waveguide-coupled spiral microring resonators with well-defined geometries can be readily obtained from foundry services (see Figure 1c). Notably, the system is compatible with the standard complementary metal oxide semiconductor (CMOS) process for mass production. The smallest feature size here, namely T , can be realized using standard deep ultraviolet (DUV) lithography, which is in contrast with previous demonstrations adopting direct-writing nanolithography for discrete nanostructures (i.e., nanonotches^[32] and nanocylinders^[33]). Without loss of generality, in our proof-of-concept demonstrations, T was chosen as ≈ 166 nm (one-third of the waveguide width W of 500 nm) and the varying θ were chosen $\approx 120.00^\circ$. Here a thermo-optic phase shifter was employed and placed on top of the ring segment between two spiral edges.

2.2. Optical Responses of Spiral Ring-Based Filters in the Vicinity of An EP

Here the mode chirality α was defined as $\alpha = (|A| - |B|)/(|A| + |B|)$ according to the two-mode approximation. In addition to an absolute strength, the sign α indicates the dominance of propagation direction in real space. According to our Hamiltonian model, the strongest chirality of 1 and -1, can be approached at EP+ and EP- respectively, via engineering both χ and θ (see Figure 2a). Optical responses can be studied by forming waveguide-based spiral ring resonators as an

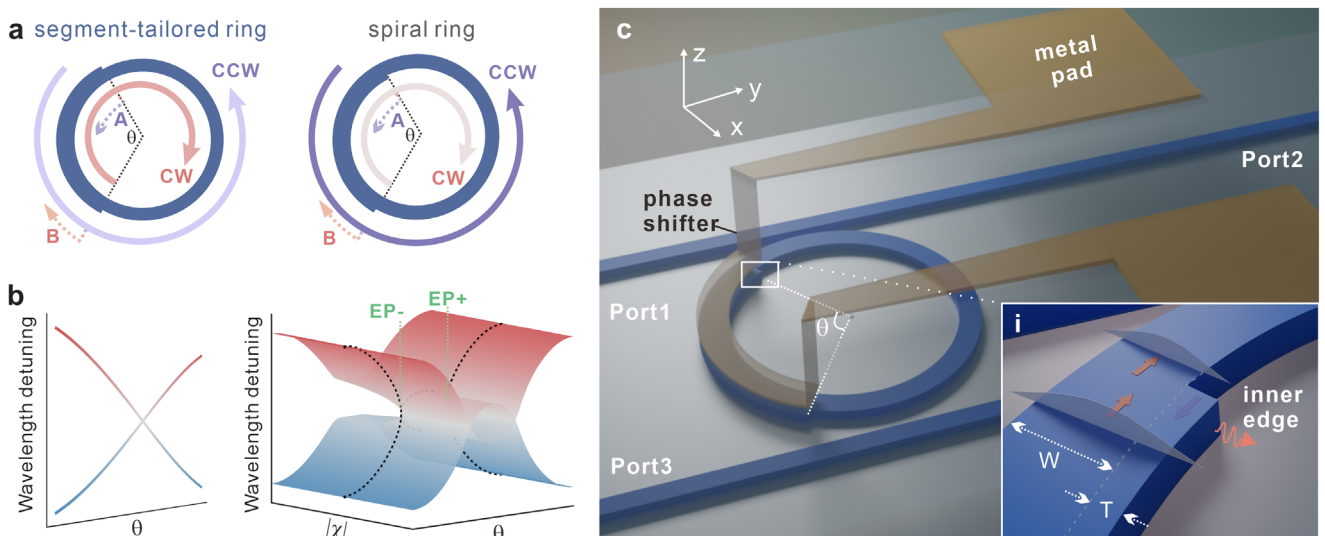


Figure 1. Schematic showing the non-Hermiticity in a spiral microring resonator. a) Schematics of a regular ring perturbed by a protruded segment with preserved mirror-symmetry (left) and a spiral ring with broken mirror-symmetry showing tunable mode chirality (right). b) Numerically calculated eigenvalues showing the resonant wavelength detuning between two non-degenerate modes in a segment-tailored ring (left) and spiral ring (right). In two systems, the azimuthal angle θ of the widened segment is the common tuning parameter. In the spiral ring, the asymmetric factor χ is an additional tuning parameter. The dashed lines represent the case where $|\chi|$ equals 1. c) Schematic of the waveguide-coupled spiral-ring-based add-drop filter with an integrated phase tuner. Inset: zoom-in view of (c) around the inner spiral edge where nonconservative coupling happens. W is the width of the ring and T is the radial offset.

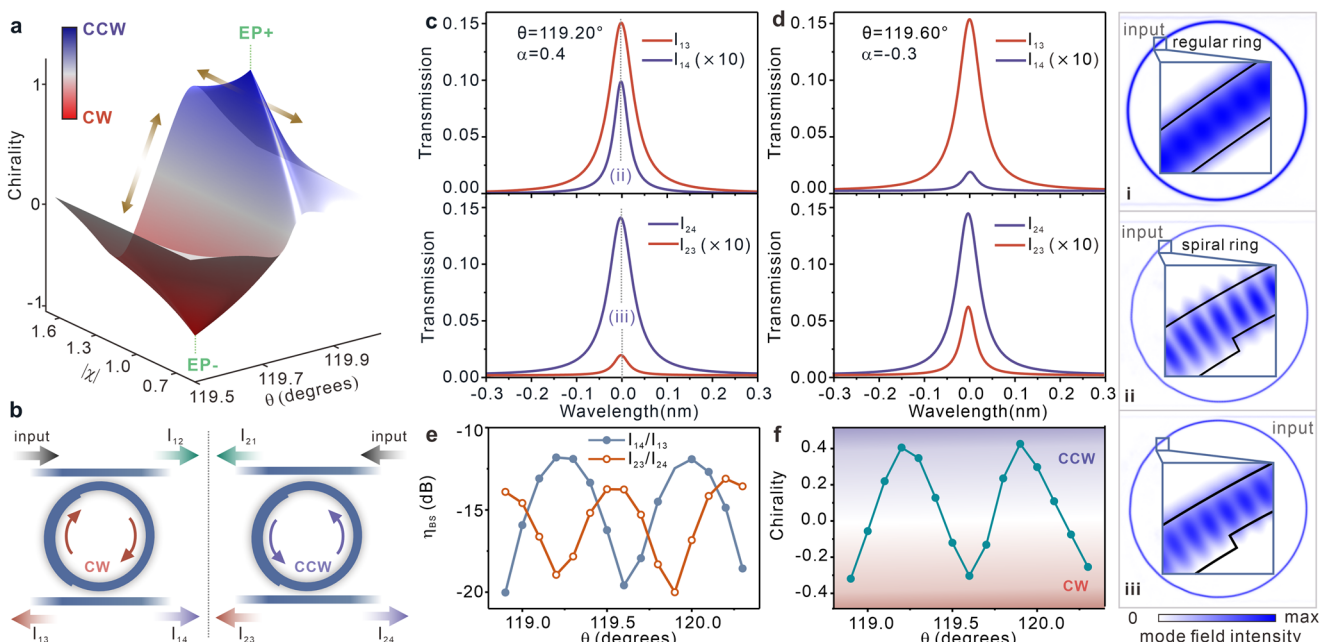


Figure 2. Theoretical studies visualizing the asymmetric backscattering in spiral rings. a) Numerically calculated surface of chirality in a $|\chi|$ - θ parameter space. b) Schematics showing light coupling from port 1 exciting in the CW direction (left) and port 2 exciting in the CCW direction (right). c) Simulated optical responses for the spiral ring with $\theta = 119.20^\circ$, showing the backscattering for excitation in the CCW direction (I_{14}) is ≈ 6 -fold stronger than that for excitation in the CW direction (I_{23}). d) Optical responses for the spiral ring with $\theta = 119.60^\circ$, showing the backscattering for excitation in the CCW direction (I_{23}) is ≈ 3.5 -fold stronger than that for excitation in the CW direction (I_{14}). Insets: simulated mode field intensity distributions at resonance wavelengths ≈ 780 nm, for (i) a regular ring excited at port 1, and (ii-iii) a spiral ring with $\theta = 119.20^\circ$ excited at port 1 (ii) and port 2 (iii). e) Summarized backscattering ratio η_{BS} as a function of θ . f) Extracted chirality α as a function of θ .

add-drop filter. Here temporal coupled mode theory (TCMT)^[45] was employed to study the spectral responses for injection from two opposite sides of the bus waveguide (i.e., ports 1 and 2, see Section S2, Supporting Information). Figure 2b illustrates the two excitation conditions, where I_{jk} denotes the intensity measured at the k^{th} port for excitation at the j^{th} port. In addition to TCMT, numerical simulations based on the finite-element method were carried out (see Experimental Section) to visualize the excited supermodes in both spectral and spatial domains.

Figure 2c,d presents the resonant spectra upon excitation at two ports for $\theta = 119.20^\circ$ and 119.60° . Transmission spectra at the throughput port (i.e., I_{12} and I_{21}) verify the preserved Lorentz reciprocity (see Section S3, Supporting Information). In contrast to previously reported microcavity systems perturbed by nano scatterers,^[26,32,46,47] no mode splitting is observed here. This is attributed to the limited coupling strength and consequently a very low “splitting quality factor” $Q_{\text{sp}} \approx 0.8$ (defined as $4g/\Gamma_{\text{sum}}$,^[48] where g is the splitting width determined by the real part of $\sqrt{\mathbf{AB}}$, and Γ_{sum} is half of the sum of linewidths for two modes).

For an ideal microring with negligible surface roughness-induced backscattering, the intensity at the add port (i.e., I_{14} here) is zero and the cavity field presents a clear traveling-wave pattern (inset i). As to spiral rings, although the signal intensities at the drop port (i.e., I_{13} and I_{24}) are comparable regardless of the excitation in the CW or CCW direction, one can discern that I_{14} and I_{23} at the same resonant wavelength differ significantly from each other (Figure 2c). Such an asymmetry of backscattering is attributed to the chiral modes with highly unbalanced weights of CCW and CW components. For a spiral ring ($\theta = 119.20^\circ$), one can discern a standing-wave feature due to the interference of co-propagating CW and CCW components (insets ii-iii). Excitation at port 1 leads to a more pronounced interference pattern (inset ii) than that of excitation at port 2 (inset iii), which is attributed to the reinforced backscattering in a chiral mode with the dominant contribution of the CCW component. Therefore, the corresponding backscattering I_{14} is enhanced while its counterpart, I_{23} , is diminished.

Notably, an opposite effect (i.e., $I_{14} < I_{23}$) can be obtained by changing θ from 119.20° to 119.60° (Figure 2d), which indicates the sign of mode chirality is flipped. As presented in Figure 2e, tuning θ results in a periodic modulation of the backscattering strength, in which the modulation period agrees with the theoretical model in Section S1 (Supporting Information). The ratio of backscattering η_{BS} for two excitation directions (i.e., I_{14}/I_{13} or I_{23}/I_{24}) oscillates between ≈ -20 and -12 dB with an opposite trend. According to TCMT theory, the chirality α can be extracted using the transmission intensities in this add-drop filter system^[26]

$$\alpha = \frac{\sqrt{I_{14}} - \sqrt{I_{23}}}{\sqrt{I_{14}} + \sqrt{I_{23}}} \quad (2)$$

As the transition point, the chirality of zero implies symmetric backscattering ($I_{14} \approx I_{23}$, and $|A| \approx |B|$) and nearly orthogonal eigenstates (see Section S3, Supporting Information). By virtue of tun-

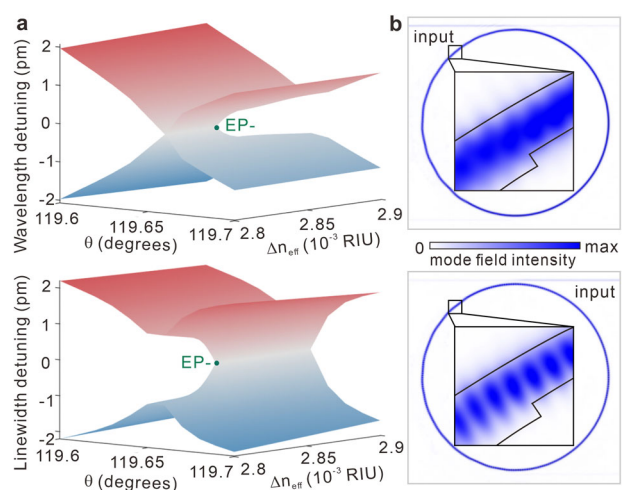


Figure 3. Steering to an EP in a spiral ring. a) The eigenvalue surfaces summarized in θ - Δn_{eff} parameter space, including the wavelength detuning (top) and the linewidth detuning (bottom). b) Simulated mode field intensity distributions at EP for a spiral ring with $\theta \approx 119.66^\circ$ excited at port 1 (top) and 2 (bottom). The extracted chirality reaches ≈ -0.95 .

ing θ , the chirality gets efficiently modulated between ≈ -0.3 and 0.4 (Figure 2f).

Despite the efficiency in tuning θ , EPs with optimal chirality of ± 1 has yet to be reached. The modeled topology of non-Hermitian degeneracies in Figure 1b also discloses the difficulty of steering to the singularity points via a single parameter. To address this, local phase tuning was employed as another control knob in manipulating the non-Hermiticity. Localized tuning of the effective refractive index n_{eff} at the segment between two spiral edges offers an alternative way of adjusting the perturbation strengths V and U for two edges, and hence effectively changes χ . As revealed in the simulated eigenmodes in a θ - Δn_{eff} parameter space (Figure 3a), an EP, the discernable branch point singularity can be reached by proper engineering of θ and Δn_{eff} . Therefore, these two tuning knobs together form a complete basis for steering toward a maximal chirality at EPs. In the simulated mode field distributions at EP (Figure 3b), the traveling-wave pattern for excitation at port 1 is in sharp contrast with the standing-wave pattern for excitation at port 2. Owing to the extremely high mode chirality, the backscattering upon excitation in the CW direction is suppressed down to ≈ -35 dB.

2.3. Characterizations of Mode Chirality by Scattering Imaging

For experimental demonstrations, a set of spiral ring-based add-drop filters was designed upon a fixed radius of $20 \mu\text{m}$ and a varying θ in the range of 118.50° and 122.00° and fabricated leveraging the multiple-project wafer (MPW) service (see Figure 4a and Experimental Section). Silicon nitride as the waveguiding material features a wide transparency window, enabling characterizations at ≈ 780 nm. Instead of collecting transmission intensity signal I_{jk} at the grating couplers using fibers, out-of-plane scattering signals at multiple ports can be simultaneously collected through an objective lens and imaged using a low-noise CMOS image sensor (see Section S4, Supporting Information).

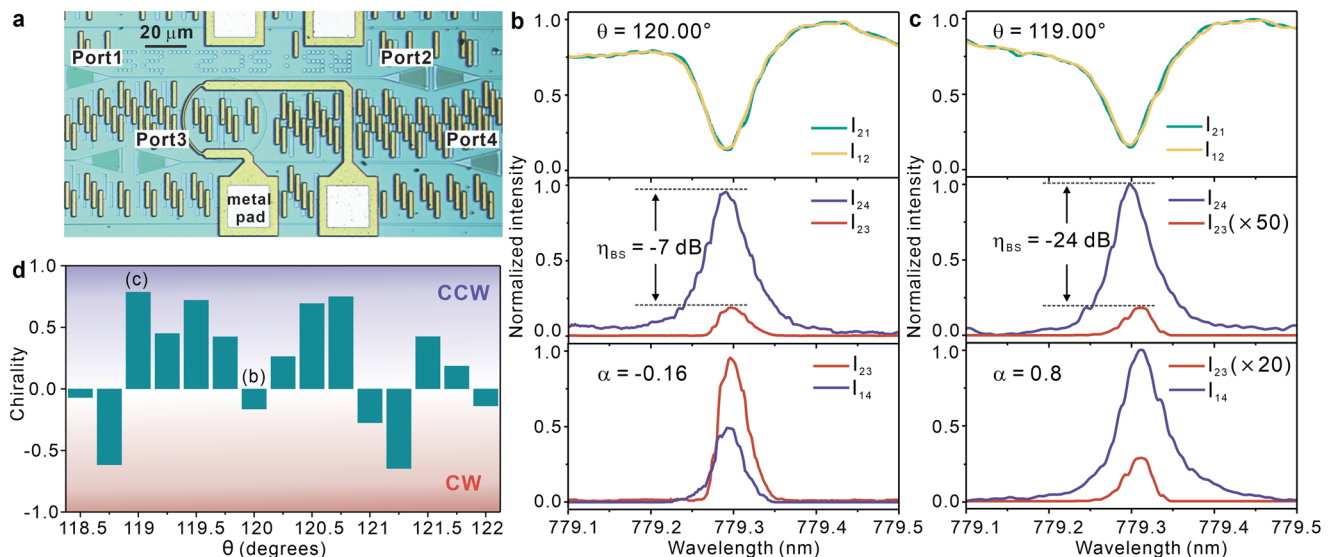


Figure 4. Characterization of mode chirality in fabricated spiral rings with varying θ . a) Optical microscope image of a spiral ring-based add-drop filter. b-c) Measured transmission spectra of I_{12} and I_{21} (top), I_{24} and I_{23} (middle), and I_{14} and I_{23} (bottom), for spiral rings with $\theta = 120.00^\circ$ (b), and $\theta = 119.00^\circ$ (c). d) Summarized relationship between the extracted chirality and θ .

Figure 4b shows the measured transmission spectra for $\theta = 120.00^\circ$. The consistency between I_{12} and I_{21} verifies Lorentz reciprocity. The moderate quality (Q) factor is attributed to the induced scattering loss at the spiral edges and potential radiation loss due to the mismatch of waveguide modes between different segments of the ring. The absence of mode splitting here agrees with the simulated results in Figure 2c,d. Due to edge-induced backscattering, η_{BS} upon excitation in the CCW direction is ≈ -7 dB. The ≈ 2 -fold higher value of I_{23} compared to I_{14} indicates a moderate asymmetry in backscattering. Besides, the extracted α of ≈ -0.16 exemplifies the co-existence of counterpropagating components. By changing θ to 119.00° (Figure 4c), one can clearly discern that η_{BS} can be optimized by ≈ -17 dB. The backscattering gets significantly mitigated while the two eigenvectors become almost collinear in the case of strong mode chirality. The contrast between I_{14} and I_{23} implies a highly asymmetric backscattering and again examines the dominant contribution of the CCW component in this chiral mode ($\alpha \approx 0.8$).

Figure 4d summarizes the measurement results of 15 samples (θ ranging from 118.50° to 122.00°) fabricated on a single block, showing a large dynamic range of α between ≈ -0.7 and ≈ 0.8 . The characterized backscattering conditions of spiral rings were compared with those of regular rings in which the intrinsic surface roughness dominates the effect (see Section S5, Supporting Information). The characterized mode chirality of regular rings is typically very weak ($|\alpha| < 0.1$). Notably, the intrinsic roughness-induced Rayleigh scattering may exhibit variations across different rings, leading to high yet probabilistic η_{BS} ranging between ≈ -9 and -2 dB. Such an uncertainty of Rayleigh scattering also accounts for the complexity of the modulation depicted in Figure 4d. By introducing the spiral geometry and edge-induced backscattering, the effect of intrinsic Rayleigh scattering can be compensated, leading to an optimized η_{BS} down to ≈ -24 dB.

2.4. Electrically Reconfiguring the Mode Chirality

Considering inevitable fabrication errors, the mode chirality in a spiral ring might not be deterministically close to a desirable value due to uncertainties in structural parameters, especially T . Under this circumstance, an efficient post-fabrication reconfiguration of mode chirality is highly desirable. In particular, the tuning of Δn_{eff} can be realized by an integrated thermal tuner module on top of the segment between two spiral edges. Upon electrical injection up to 60 mW, the tracked transmission spectra in Figure 5a reveal a spectral redshift $\Delta\lambda_{res}$ up to ≈ 0.42 nm (corresponding to Δn_{eff} of ≈ 0.0031 RIU). For spectra with reversed excitation directions, the evolution of asymmetry in backscattering upon an increased injection power can be explicitly revealed, corresponding to reconfigured chirality from ≈ -0.2 to 0.6 (Figure 5b). Simulation results in Figure 5c present that the chirality continuously increases from ≈ -0.1 to 0.5 upon Δn_{eff} of ≈ 0.004 RIU.

Given the augmented chirality, experimentally characterized η_{BS} for excitation in the CCW direction was optimized from -7 to -18 dB (Figure 5d), while the simulated results suggest the optimized value from ≈ -14 to -20 dB (Figure 5e). During this reconfiguration process, the extracted Q factor at strong chirality (power of 60 mW) gets improved by 15% compared to that at a weak chirality (power of 30 mW), which further ascertains the suppression of mode splitting width g (see Section S6, Supporting Information). Notably, electrical reconfiguration enables not only sign-reversing of chirality but also reinforced chirality approaching an EP (see Section S6, Supporting Information for a characterized maximal chirality of ≈ 0.86).

In view of the deviation between experimental and simulation results in Figures 2, 3 and 5, one should note that numerical simulations cannot serve as a direct prediction of the performance of experimentally realized devices due to the uncertainties of

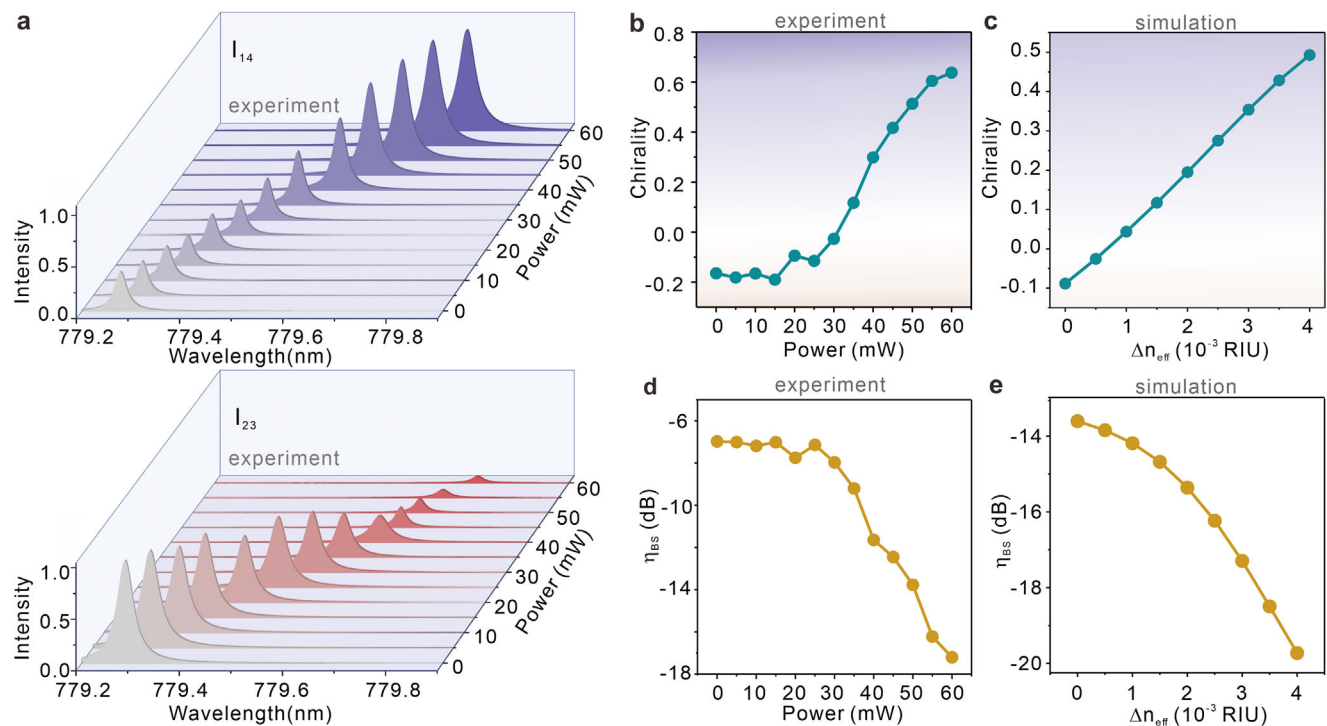


Figure 5. Characterization of electrically reconfigurable mode chirality. a) Lorentzian fits of resonant spectra upon an increased injection power for I_{14} (top) and I_{23} (bottom) in a spiral ring with $\theta = 120.00^\circ$. b) Extracted chirality as a function of the injection power. c) Extracted chirality as a function of Δn_{eff} . d) Extracted η_{BS} as a function of the injection power. e) Extracted η_{BS} as a function of Δn_{eff} .

geometry in actual fabrications. In our tolerance analysis (see Section S7, Supporting Information), the effect on the variance of T in actual fabrications was carefully studied. Considering $\Delta T = \pm 20$ nm at the very least, the mode chirality can be efficiently manipulated using θ . Therefore, there are no challenges arising from the constraints of dimensions, which is advantageous compared with the required precision in the dimensions of nanostructures and potential susceptibility in the reported “two-scatterers” approach for WGM microcavities.^[28,32]

3. Conclusion

In this work, we proposed and demonstrated strong yet reconfigurable mode chirality in spiral microring resonators. Through benchmarking with previous experimental studies on chiral modes in microrings and other WGM microcavities (see Supporting Information Section 8), we report to our knowledge the first demonstration of reconfigurable mode chirality in integrated optical microresonators. Besides, the full process was implemented using solely on-chip integrated modules leveraging mature foundry services. The non-Hermiticity in the spiral microring system can be manipulated by tuning the relative spacing between two spiral edges, leading to the experimental observation of strong chirality up to ≈ 0.86 . Compared with regular microrings with probabilistic non-Hermiticity due to fabrication imperfections, the originally Rayleigh scattering-dominated backscattering can be suppressed with η_{BS} down to ≈ -24 dB. Besides, an integrated phase tuner was pivoted as a control knob to steer toward or away from EPs and the correlated maximal chirality. Elec-

trical re-configuration of the chirality has been corroborated by both experimental and simulation results.

All in all, we envision that the formulated insights in spiral ring resonators will serve as a bridge that connects peculiar behaviors in non-Hermitian photonics with various functional devices in optoelectronic integrated circuits. Such integrated microring resonators with electrically reconfigurable mode chirality have great potential as generic optically passive and active building blocks, shaping the light flow and emission on a chip for optical signal processing in both classical^[49] and quantum^[6,50,51] regimes. This finding may further spark a surge of chiral EP-enabled functionalities, such as enhanced sensing,^[28] unidirectional and reconfigurable emissions,^[16,17,52] non-reciprocity,^[5] and chiral perfect absorption.^[53]

4. Experimental Section

Numerical Simulation: Numerical simulations were performed based on the finite-element method (COMSOL Multiphysics, wave-optics module). Limited by the computation power, 2D modeling was adopted. The device geometry in the simulation follows exactly with the fabricated ones ($W = 500$ nm, $T = 166$ nm, and $R = 20$ μm). The effective refractive index n_{eff} was set as $\approx 1.7 + 3 \times 10^{-7}i$, in which the real part takes into account the confinement in the vertical dimension through boundary mode analysis, and the imaginary part was introduced considering the waveguide propagation loss (≈ 0.2 dB cm^{-1}). While the input port was excited using transverse electric (TE)-polarized light, transmission spectra at the other three ports can be collected by wavelength sweeping (step of 2 pm). Fine meshing condition was applied to the waveguide and microring region (grid size of ≈ 20 nm). Besides, for understanding the inter-modal coupling

and non-Hermiticity, a pair of eigenvalues and eigenstates was calculated using the eigenmode solver.

Device Fabrication: Waveguide-coupled microring resonators were fabricated on a silicon-nitride-on-silica platform in a single block of $\approx 10 \times 5$ mm by an MPW service (AN150, LIGENTEC). The layout was prepared using a photonic integrated circuit design software (IPKISS, Luceda) leveraging the foundry PDK. For single-mode propagation at ≈ 780 nm, the waveguiding SiN layer thickness was chosen as 150 nm, and the waveguide width was chosen as 500 nm. The aluminum-based phase shifter was integrated on the segment between the two spiral edges, which offers a phase tuning up to $\approx 0.54\pi$ due to the thermo-optic effect.

Device Characterization: The wavelength-tunable laser light (TLB-6712, Newport) at ≈ 780 nm was coupled into a single-mode fiber using free-space optics. The polarization was adjusted by a fiber-based polarization controller. The waveguide-coupled microring resonators were probed by grating couplers, and characterized by two fibers with the assistance of a high-precision aligning system with a feedback loop (AP-SSAS-SIP-SAXYZ, Apico). Transmission signals were measured using an optical power meter (PM100D, Thorlabs). For imaging of out-of-plane scattered light, a long-working-distance microscope objective lens (10x Mitutoyo Plan Apo, NA = 0.28) and a monochrome sCMOS camera (CS2100M-USB, Thorlabs) with 1080×1920 pixels (pixel size of $5.04 \times 5.04 \mu\text{m}$) were employed. The optical power being scattered at the drop port was estimated to be ≈ 10 pW or less. The exposure time was adjusted between 1 and 200 ms to avoid signal saturation. For electrical reconfiguration of chirality, bias voltage was applied via two probes using a source meter (S100, Precise). The calibrated tuning efficiency was $\approx 5.2 \times 10^{-5}$ RIU mW $^{-1}$.

Supporting Information

Supporting Information is available from the Wiley Online Library or from the author.

Acknowledgements

J.W. acknowledges the support from the National Natural Science Foundation of China (NSFC) under Grants U22A2093, 62105080 and 62211530431, the Guangdong Basic and Applied Basic Research Foundation Regional Joint Fund under Grants 2020B1515130006, 2021B515120056 and 2023A1515011944, the Science and Technology Innovation Commission of Shenzhen under Grants JCYJ20220531095604009 and RCYX20221008092907027.

Conflict of Interest

The authors declare no conflict of interest.

Author Contributions

Y.C. and J.L. contributed equally to this work. J.W. and X.C.X. conceived the idea. J.L., S.B., and R.F. performed the theoretical analysis and numerical modeling; Y.C., K.X., X.W., and J.D. designed the devices and conducted the experiments; Y.C. and J.L. performed the data analysis with the assistance of C.H.; J.W., L.P., and X.C.X. supervised the project; J.W. and J.L. wrote the manuscript; All authors discussed the results and contributed to the manuscript.

Data Availability Statement

The data that support the findings of this study are available from the corresponding author upon reasonable request.

Keywords

Chirality, exceptional point, microresonators, non-hermitian

Received: December 6, 2023

Revised: May 20, 2024

Published online: June 11, 2024

- [1] J. Wang, S. C. Zhang, *Nat. Mater.* **2017**, *16*, 1062.
- [2] S.-H. Yang, R. Naaman, Y. Paltiel, S. S. P. Parkin, *Nat. Rev. Phys.* **2021**, *3*, 328.
- [3] P. Lodahl, S. Mahmoodian, S. Stobbe, A. Rauschenbeutel, P. Schneeweiss, J. Volz, H. Pichler, P. Zoller, *Nature* **2017**, *541*, 473.
- [4] M. Parto, H. Lopez-Aviles, J. E. Antonio-Lopez, M. Khajavikhan, R. Amezcua-Correa, D. N. Christodoulides, *Sci. Adv.* **2019**, *5*, eaau8135.
- [5] A. Muñoz de las Heras, R. Franchi, S. Biasi, M. Ghulinyan, L. Pavesi, I. Carusotto, *Phys. Rev. Appl.* **2021**, *15*, 054044.
- [6] L. Tang, J. Tang, W. Zhang, G. Lu, H. Zhang, Y. Zhang, K. Xia, M. Xiao, *Phys. Rev. A* **2019**, *99*, 043833.
- [7] S. Soleymani, Q. Zhong, M. Mokim, S. Rotter, R. El-Ganainy, S. K. Ozdemir, *Nat. Commun.* **2022**, *13*, 599.
- [8] J. Doppler, A. A. Mailybaev, J. Böhm, U. Kuhl, A. Girschik, F. Libisch, T. J. Milburn, P. Rabl, N. Moiseyev, S. Rotter, *Nature* **2016**, *537*, 76.
- [9] H. Cao, J. Wiersig, *Rev. Mod. Phys.* **2015**, *87*, 61.
- [10] C. Wang, Z. Fu, W. Mao, J. Qie, A. D. Stone, L. Yang, *Adv. Opt. Photonics* **2023**, *15*, 442.
- [11] R. El-Ganainy, K. G. Makris, M. Khajavikhan, Z. H. Musslimani, S. Rotter, D. N. Christodoulides, *Nat. Phys.* **2018**, *14*, 11.
- [12] A. Li, H. Wei, M. Cotrufo, W. Chen, S. Mann, X. Ni, B. Xu, J. Chen, J. Wang, S. Fan, C. W. Qiu, A. Alu, L. Chen, *Nat. Nanotechnol.* **2023**, *18*, 706.
- [13] K. Y. Bliokh, F. J. Rodríguez-Fortuño, F. Nori, A. V. Zayats, *Nat. Photonics* **2015**, *9*, 796.
- [14] R. Sarma, L. Ge, J. Wiersig, H. Cao, *Phys. Rev. Lett.* **2015**, *114*, 053903.
- [15] J. Wang, M. Tang, Y.-D. Yang, Y. Yin, Y. Chen, C. N. Saggau, M. Zhu, X. Yuan, D. Karnaushenko, Y.-Z. Huang, L. Ma, O. G. Schmidt, *Laser Photonics Rev.* **2020**, *14*, 2000118.
- [16] Q.-T. Cao, R. Liu, H. Wang, Y.-K. Lu, C.-W. Qiu, S. Rotter, Q. Gong, Y.-F. Xiao, *Nat. Commun.* **2020**, *11*, 1136.
- [17] L. Del Bino, J. M. Silver, S. L. Stebbings, P. Del'Haye, *Sci. Rep.* **2017**, *7*, 43142.
- [18] Z. Zhang, X. Qiao, B. Midya, K. Liu, J. Sun, T. Wu, W. Liu, R. Agarwal, J. M. Jornet, S. Longhi, *Science* **2020**, *368*, 760.
- [19] Z. Zhang, H. Zhao, D. G. Pires, X. Qiao, Z. Gao, J. M. Jornet, S. Longhi, N. M. Litchinitser, L. Feng, *Light Sci. Appl.* **2020**, *9*, 179.
- [20] N. Zhang, Z. Gu, S. Liu, Y. Wang, S. Wang, Z. Duan, W. Sun, Y.-F. Xiao, S. Xiao, Q. Song, *Optica* **2017**, *4*, 1151.
- [21] G. Q. Qin, R. R. Xie, H. Zhang, Y. Q. Hu, M. Wang, G. Q. Li, H. Xu, F. Lei, D. Ruan, G. L. Long, *Laser Photonics Rev.* **2021**, *15*, 2000569.
- [22] C. Wang, W. R. Sweeney, A. D. Stone, L. Yang, *Science* **2021**, *373*, 1261.
- [23] M. A. Miri, A. Alu, *Science* **2019**, *363*, eaar7709.
- [24] J. Wiersig, *Phys. Rev. Lett.* **2014**, *112*, 203901.
- [25] J. Wiersig, *Phys. Rev. A* **2016**, *93*, 033809.
- [26] B. Peng, S. K. Ozdemir, M. Lierterzer, W. Chen, J. Kramer, H. Yilmaz, J. Wiersig, S. Rotter, L. Yang, *Proc. Natl. Acad. Sci. USA* **2016**, *113*, 6845.
- [27] J. Zhu, S. K. Özdemir, L. He, L. Yang, *Opt. Express* **2010**, *18*, 23535.
- [28] W. Chen, S. Kaya Ozdemir, G. Zhao, J. Wiersig, L. Yang, *Nature* **2017**, *548*, 192.
- [29] J. Qie, C. Wang, L. Yang, *Laser Photonics Rev.* **2023**, *17*, 2200717.
- [30] A. O. Svela, J. M. Silver, L. Del Bino, S. Zhang, M. T. M. Woodley, M. R. Vanner, P. Del'Haye, *Light Sci. Appl.* **2020**, *9*, 204.

- [31] A. Mazzei, S. Gotzinger, S. Menezes Lde, G. Zumofen, O. Benson, V. Sandoghdar, *Phys. Rev. Lett.* **2007**, 99, 173603.
- [32] H. Lee, A. Kecebas, F. Wang, L. Chang, S. K. Özdemir, T. Gu, *eLight* **2023**, 3, 20.
- [33] J. Li, W. Li, Y. Feng, J. Wang, Y. Yao, Y. Sun, Y. Zou, J. Wang, F. He, J. Duan, *Nano Lett.* **2024**, 24, 3906.
- [34] A. Calabrese, F. Ramiro-Manzano, H. M. Price, S. Biasi, M. Bernard, M. Ghulinyan, I. Carusotto, L. Pavesi, *Photon. Res.* **2020**, 8, 1333.
- [35] W. E. Hayenga, M. Parto, J. Ren, F. O. Wu, M. P. Hokmabadi, C. Wolff, R. El-Ganainy, N. A. Mortensen, D. N. Christodoulides, M. Khajavikhan, *ACS Photonics* **2019**, 6, 1895.
- [36] R. Franchi, S. Biasi, D. Piciocchi, L. Pavesi, *APL Photonics* **2023**, 8, 056111.
- [37] Q. Zhong, J. Ren, M. Khajavikhan, D. N. Christodoulides, S. K. Özdemir, R. El-Ganainy, *Phys. Rev. Lett.* **2019**, 122, 153902.
- [38] W. Li, Y. Zhou, P. Han, X. Chang, S. Jiang, A. Huang, H. Zhang, Z. Xiao, *Phys. Rev. A* **2021**, 104, 033505.
- [39] K. Liao, Y. Zhong, Z. Du, G. Liu, C. Li, X. Wu, C. Deng, C. Lu, X. Wang, C. T. Chan, Q. Song, S. Wang, X. Liu, X. Hu, Q. Gong, *Sci. Adv.* **2023**, 9, eadbf3470.
- [40] M. A. Tran, C. Zhang, T. J. Morin, L. Chang, S. Barik, Z. Yuan, W. Lee, G. Kim, A. Malik, Z. Zhang, *Nature* **2022**, 610, 54.
- [41] J. K. Poon, A. Govdeli, A. Sharma, X. Mu, F.-D. Chen, T. Xue, T. Liu, *Adv. Opt. Photonics* **2024**, 16, 1.
- [42] J. Wang, Z. Yao, A. W. Poon, *Fron. Mater.* **2015**, 2, 34.
- [43] J. Li, M. Tang, J. Duan, X. Xu, K. Xu, L. Ma, J. Wang, *J. Light. Technol.* **2023**, 41, 2870.
- [44] J. Wiersig, *Phys. Rev. A* **2011**, 84, 063828.
- [45] S. Wonjoo, W. Zheng, F. Shanhui, *IEEE J. Quantum Electron.* **2004**, 40, 1511.
- [46] Y. Xu, S.-J. Tang, X.-C. Yu, Y.-L. Chen, D. Yang, Q. Gong, Y.-F. Xiao, *Phys. Rev. A* **2018**, 97, 063828.
- [47] J. Zhu, S. K. Ozdemir, Y.-F. Xiao, L. Li, L. He, D.-R. Chen, L. Yang, *Nat. Photonics* **2009**, 4, 46.
- [48] Ş. K. Özdemir, J. Zhu, L. He, L. Yang, *Phys. Rev. A* **2011**, 83, 033817.
- [49] G. Liang, H. Huang, A. Mohanty, M. C. Shin, X. Ji, M. J. Carter, S. Shrestha, M. Lipson, N. Yu, *Nat. Photonics* **2021**, 15, 908.
- [50] Q. Zhong, A. Hashemi, Ş. K. Özdemir, R. El-Ganainy, *Phys. Rev. Res.* **2021**, 3, 013220.
- [51] R. Huang, Ş. K. Özdemir, J. Q. Liao, F. Minganti, L. M. Kuang, F. Nori, H. Jing, *Laser Photonics Rev.* **2022**, 16, 2100430.
- [52] A. Muñoz de las Heras, I. Carusotto, *Phys. Rev. A* **2021**, 104, 043501.
- [53] W. R. Sweeney, C. W. Hsu, S. Rotter, A. D. Stone, *Phys. Rev. Lett.* **2019**, 122, 093901.